Full length article

On the origin of the improvement of shape memory effect by precipitating VC in Fe−Mn−Si-based shape memory alloys

M.J. Lai [a, *], Y.J. Li [a, b], L. Lillpopp [c], D. Ponge [a, **], S. Will [c], D. Raabe [a]

[a] Max-Planck-Institut für Eisenforschung GmbH, Max-Planck-Str. 1, 40237, Düsseldorf, Germany
[b] ZGH, Ruhr-Universität Bochum, Universitätsstr. 150, 44780, Bochum, Germany
[c] thyssenkrupp Steel Europe AG, Kaiser-Wilhelm-Str. 100, 47166, Duisburg, Germany

A B S T R A C T

We studied the role of VC precipitation in improving the shape memory effect (SME) of the as-solution treated Fe−Mn−Si-based shape memory alloys by examining the microstructures developed during aging and deformation using transmission electron microscopy and electron channeling contrast imaging. Our results suggest that VC particles are not the only product of aging. Upon aging at 650 °C, the precipitation of VC particles is accompanied by the formation of profuse dislocations $(2.26 \pm 0.098 \times 10^{13} \, \text{m}^{-2})$. In this case, the SME is not improved compared to the as-solution treated reference state. Upon aging at high temperatures (700−900 °C), a number of stacking faults are formed accompanying the VC precipitation and the SME is significantly improved, where the recovery ratios reach almost twice that of the as-solution treated state (<50%). For these high-temperature aged states, in situ straining experiments reveal that the stacking faults rather than the VC particles play an important role in the stress-induced martensitic transformation, leading to the formation of very thin (<3 nm) martensite plates with a single crystallographic variant within each grain. These martensite plates are in contrast to the very thick (from tens to hundreds of nanometers) and multi-variant martensite plates that prevail in the as-solution treated state. By comparing the characteristics of the martensite plates between the as-solution treated and the high-temperature aged states, the reasons for the improvement of SME by precipitating VC were discussed.

© 2018 Acta Materialia Inc. Published by Elsevier Ltd. All rights reserved.

1. Introduction

Shape memory alloys are characterized by reversible diffusionless/martensitic transformation, i.e., stress-induced martensitic transformation upon loading and its reverse transformation upon unloading or heating [1,2]. In deformed shape memory alloys, a certain portion of the non-linear strain can be recovered upon unloading and further recovery can be attained by heating above a critical temperature. The former phenomenon is referred to as superelasticity and the latter shape memory effect (SME) [3]. Both phenomena arise from the reverse martensitic transformation. In the past half century, Ti−Ni-based alloys have attracted the most extensive research efforts among all shape memory alloys owing to their excellent superelasticity and SME

(recovery strain up to 8%) as well as the associated complicated martensitic transformations [4−6]. Numerous applications such as pipe couplings, coronary stents and micro-actuators [7−10] have been found for Ti−Ni-based shape memory alloys. Nevertheless, these alloys suffer from high alloying costs and low workability, limiting their wider application.

In 1982, Sato et al. [11] observed a large recovery strain (up to 9%) comparable to that of Ti−Ni-based shape memory alloys in single-crystalline Fe−30Mn−1Si alloy, opening up the possibility of developing commercially more attractive ferrous shape memory alloys with lower alloying costs and better workability. However, subsequent studies [12−14] revealed that the as-solution treated polycrystalline Fe−Mn−Si-based alloys suffered from a low recovery strain. Even the three alloys, Fe−28Mn−6Si−5Cr, Fe−20Mn−5Si−8Cr−5Ni and Fe−16Mn−5Si−12Cr−5Ni, which were claimed to have a combination of good corrosion resistance and good SME, exhibited a recovery strain <2.5% [13]. In the past three decades, considerable effort has been devoted to improving the SME of these alloys and their derivatives [13−32].

* Corresponding author.
** Corresponding author.
  E-mail addresses: m.lai@mpie.de (M.J. Lai), d.ponge@mpie.de (D. Ponge).

Given that the SME of the Fe−Mn−Si-based alloys arises from the reversible transformation between face-centered cubic (fcc) γ austenite and hexagonal close-packed (hcp) ε martensite, all factors that promote the γ → ε martensitic transformation during straining or the reverse ε → γ transformation during heating are likely to improve the SME. In addition, the factors that increase the yield strength of the parent austenite are also considered effective in terms of preventing the undesired intrusion of irreversible slip deformation during martensitic transformation. The majority of the initial attempts to realize these beneficial factors were focused on thermomechanical treatments: (i) ausforming, i.e., performing slight tensile deformation above the temperature for martensitic transformation [15,17,19]; and (ii) training, i.e., imposing a few cycles of slight deformation at room temperature and subsequent recovery annealing [13,16,18]. These two types of treatment have indeed led to increased recovery strains, e.g., 3.8% in an ausformed Fe−29.9Mn−6Si alloy [19] and 5.4% in a trained Fe−20Mn−6Si−7Cr−1Cu alloy [18]. Such improvements in the attained SME were initially attributed to the enhancement of the yield strength of the austenite as well as to the reduction of the critical stress for martensitic transformation [13,19].

By correlating the SME to the characteristic features of the stress-induced martensite plates, Kajiwara et al. [33−36] proposed that in trained Fe−Mn−Si-based alloys the improvement of SME was governed by the formation of (i) uniformly distributed, (ii) very thin (~1 nm in thickness) and (iii) single-variant martensite plates within each grain. The training-induced increase in the yield strength of the austenite and decrease in the critical stress for martensitic transformation were regarded as a necessary but not sufficient condition for improving the SME. The characteristic microstructures developed during training were identified as high densities of uniformly distributed stacking faults (SFs) [33,36,37] and very thin hcp plates [36] on the primary slip planes of the austenite. These microstructures were considered indispensable for the formation of the specific martensite plates mentioned above upon mechanical loading to reach a shape change [33−36]. In the alloys subjected to ausforming, uniformly distributed SFs have also been observed [20] and the formation of thin martensite plates with the same variant has also been considered to play the dominant role in improving the SME [38].

It should be noted that additional thermomechanical treatments raise the processing costs and they are not applicable for complicated shapes. In 2001, Kajiwara et al. [21,22] reported a remarkable increase in the recovery strain by precipitating fine NbC particles in Fe−Mn−Si-based alloys without applying any additional training. Subsequent studies suggested that the precipitation of VN [26,27], TiC [39,40] and VC [30,31] also resulted in the improvement of SME. All of these precipitates have a NaCl-type crystal structure, identical to that of NbC. In addition to increasing the yield strength of the austenite via precipitation hardening, these precipitates have been speculated (i) to act as the nucleation sites of stress-induced martensite [21,22,24−27,39,40], i.e., promoting the stress-induced γ → ε martensitic transformation, and (ii) to exert back stresses to the martensite tips that approach them [21,24,26,27]. Such back stresses, which result from the elastic strain field surrounding the precipitates, were supposed to assist the reverse movement of the Shockley partial dislocations at the martensite tips during recovery annealing, i.e., promoting the reverse ε → γ transformation. However, to date no direct experimental evidence is available to justify these speculations. On the other hand, the work of Stanford and Dunne [39,40] suggested that under certain circumstances precipitates did not necessarily lead to the improvement of SME, e.g., for rather small NbC precipitates (<5 nm) even a detrimental effect was observed. Therefore, a fundamental understanding concerning the influence of the precipitates on the SME, especially the origin for the improvement of SME by precipitation, remains to be developed.

Here, we investigate the role of VC precipitation in improving the SME of an as-solution treated Fe−28Mn−6Si−5Cr−0.764V−0.18C (wt.%) alloy. Aging treatments are carried out at various temperatures for precipitating VC and bending tests are performed to assess the SME. We examine the microstructures developed during aging and the stress-induced martensite plates formed during deformation using transmission electron microscopy (TEM). In situ observation of the evolution of the martensite plates during straining is made using electron channeling contrast imaging (ECCI) [41]. We discuss the contribution of the VC precipitation to the improvement of SME based on the comparison of the following three aspects between the as-solution treated and the aged samples: (i) the initial microstructures, (ii) the martensite plates and (iii) the evolution of these plates.

2. Experimental

The as-received hot-rolled alloy sheets were solution treated at 1140 °C for 6 h under argon atmosphere and subsequently water quenched to room temperature. Their chemical composition was analyzed by inductively coupled plasma optical emission spectroscopy, Table 1. For precipitating VC, a few of the as-solution treated sheets were aged at 650−900 °C for 2 h under argon atmosphere and then subjected to water quenching. All specimens for the following experiments were cut from the as-solution treated or aged sheets by electrical discharge machining.

The SME was measured using bending tests and recovery annealing. Flat specimens with their longitudinal direction parallel to the rolling direction of the sheets and a dimension of $100 \times 2 \times 1$ mm³ were bent around various bend radii to produce a series of pre-strains. The bending pre-strain ε_p was determined by the following equation [39]:

$$\varepsilon_p = \frac{t}{2R + t}, \tag{1}$$

where t and R are specimen thickness and bend radius, respectively. The shape recovery of the bent specimens was accomplished by annealing at 450 °C for 15 min. Subsequently, the residual strain ε_r resulting from incomplete recovery was estimated using Eq. (1) as well. The recovery ratio was given by $(\varepsilon_p - \varepsilon_r)/\varepsilon_p \times 100\%$, where $(\varepsilon_p - \varepsilon_r)$ is the recovery strain.

For characterizing the stress-induced martensite plates in detail, flat dog-bone shaped tensile specimens with a gauge section of $20 \times 5 \times 2$ mm³ were cut along the rolling direction of the sheets. They were deformed to 4% total strain under tension at a cross-head speed of 0.6 mm/min (corresponding to an initial strain rate of 5×10^{-4} s⁻¹) in a Zwick ZH 100 tensile testing machine. An extensometer was used to record the tensile strain. After deformation, round TEM disks with a diameter of 3 mm and a thickness of 0.5 mm were cut from the gauge section of the deformed tensile specimens. The evolution of the stress-induced martensite plates was examined by in situ three-point bending experiments performed in a scanning electron microscope (SEM), where flat specimens with a dimension of $7 \times 3.5 \times 0.8$ mm³ were used. One 7×0.8 mm² surface of these specimens was polished prior to deformation. On such a surface sequential microstructural

Table 1
Chemical composition (wt.%) of the as-solution treated alloy.

Element	Fe	Mn	Si	Cr	V	C
Composition	Balance	27.9	5.68	5.16	0.773	0.212

observation was carried out by interrupting the bending experiment at various strain levels.

Specimens for electron backscatter diffraction (EBSD) analysis and ECCI observation were first ground using SiC papers up to 4000 grit and then polished for ~10 min using diamond suspension (~3 μm), followed by a final precision polishing using a 50−100 nm colloidal silica suspension neutralized by H_2O_2. EBSD mapping was carried out in a Zeiss Crossbeam XB 1540 field emission gun SEM (equipped with TSL/EDAX OIM v6) operated at 15 kV, while ECCI observation was performed in a Zeiss MERLIN field emission gun SEM operated at 30 kV. X-ray diffraction (XRD) analysis was carried out using Co-K_α radiation ($\lambda = 1.78897$ Å) over a 2θ range from 30° to 130° at a scanning speed of 0.3°/min. Atom probe tomography (APT) analysis was conducted in a local electrode atom probe (LEAP 3000X HR, CAMECA Instruments Inc.) operated in voltage mode at 75 K and 0.005 atom/pulse detection rate. The amplitude of voltage pulse was 15% and the pulse frequency was 200 kHz. Needle-shaped APT specimens were prepared using a dual-beam focused ion beam (FIB) workstation (FEI Helios Nanolab 600). For TEM analysis, round TEM disks were first ground down to a thickness of ~120 μm using SiC papers up to 4000 grit and then further thinned by twin-jet electropolishing (Struers Tenupol 5) at −30 °C and 24 V until perforation using an electrolyte of 5% perchloric acid in ethanol. Site-specific FIB lift-out TEM lamellae were prepared as well using FEI Helios Nanolab 600 through a process as described in Ref. [42]. TEM observation was conducted in a JEOL JEM-2200FS microscope operated at 200 kV.

3. Results

3.1. Initial microstructures of the as-solution treated state

Fig. 1 shows the initial microstructures of the as-solution treated alloy sheets. The EBSD analysis reveals a single fcc γ phase with equiaxed grain structures (Fig. 1a). The average grain size is 580 μm and most of the grains contain annealing twins. The ratio of the length of twin boundaries (L_{TB}) to the total length of both grain boundaries and twin boundaries (L_{GB+TB}) is 47.81%. The pole figures of Fig. 1b show randomly distributed multiple intensity maxima, revealing a random texture. At a smaller scale, the scanning transmission electron microscopy (STEM) observation illustrates that the γ grains contain few SFs and a rather low density of dislocations before the aging treatments, as shown in Fig. 1c. The

selected area diffraction (SAD) pattern, inset of Fig. 1c, reveals only one set of diffraction spots from the [110] zone axis of the γ phase, demonstrating that the as-solution treated alloy consists of a single phase.

3.2. Precipitation of VC

For the temperature range of 650−900 °C, thermodynamic calculations predict that the equilibrium volume fraction of the VC precipitate is in the range of 1.17−1.37 vol.% and exhibits a slightly decreasing trend with increasing temperature (Supplementary Fig. S1). EBSD analysis reveals that aging at this temperature range for 2 h has little effect on the grain size, L_{TB}/L_{GB+TB} and texture of the alloy sheets. The precipitation of VC after such aging treatments was examined by TEM analysis. Fig. 2 displays the representative microstructures developed during aging at 650 °C. Profuse dislocations are generated as shown in Fig. 2a, very few of which have already dissociated to form recognizable SFs. The dislocation density was estimated to be $2.26 \pm 0.098 \times 10^{13}$ m^{-2} using the method described in Ref. [43]. The inset of Fig. 2a illustrates that there are uniformly distributed extremely small particles (~6 nm) within the γ matrix and the dislocations are decorated by somewhat larger particles. These particles were identified as VC by high resolution transmission electron microscopy (HRTEM) analysis as shown in Fig. 2b–d. The red arrows in Fig. 2b indicate three VC particles, within which translational moiré fringes parallel to $(\bar{1}11)_\gamma$ and $(\bar{1}1\bar{1})_\gamma$ planes are shown. The intersection of these two sets of fringes gives rise to strawberry-like contrast, resembling that of VN [27]. The orientation relationship between fcc γ and NaCl-type VC, as determined by the fast Fourier transform (FFT) pattern (Fig. 2c), is $[110]_\gamma//[110]_{VC}$ and $(001)_\gamma//(001)_{VC}$, i.e., of cube-cube orientation relationship. The translational moiré fringes, thus, arise from the difference in {111} lattice spacing between γ and VC [44]. In the FFT pattern, it should be noted that besides the primary diffraction spots from γ and VC, as schematically illustrated in Fig. 2d, additional diffraction spots resulting from double diffraction are observed close to the primary spots and also to the transmitted spot. This is a normal diffraction phenomenon associated with moiré fringes [44].

The characteristic microstructures developed at higher aging temperatures (≥700 °C) are shown in Fig. 3, where all images are viewed along the $[110]_\gamma$ direction and the corresponding SAD patterns reveal only two phases, i.e., γ and VC. An example of the SAD
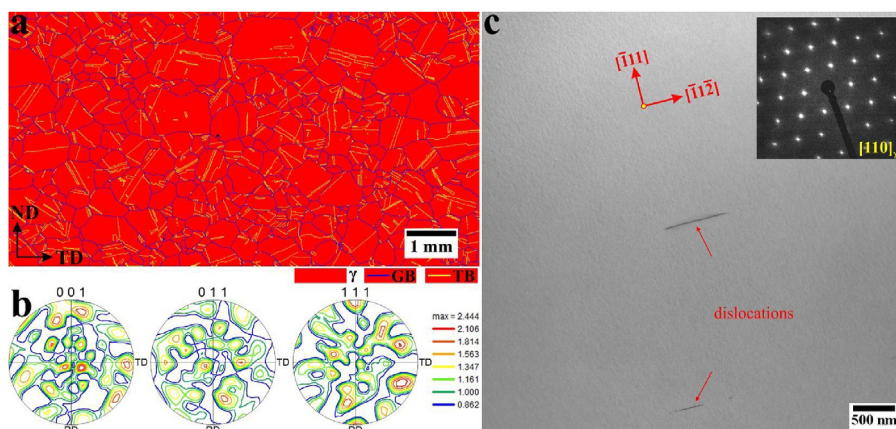

Fig. 1. Initial microstructures of the as-solution treated alloy sheets. (a) EBSD phase map where the blue and yellow lines represent the positions of the grain boundaries (GBs) and of the annealing twin boundaries (TBs), respectively. (b) EBSD pole figures with the alloy sheet normal direction (ND) at the center. The rolling direction (RD) and transverse direction (TD) are shown. (c) STEM bright field image viewed along the $[110]_\gamma$ direction with an inset showing the corresponding SAD pattern. (For interpretation of the references to color in this figure legend, the reader is referred to the Web version of this article.)
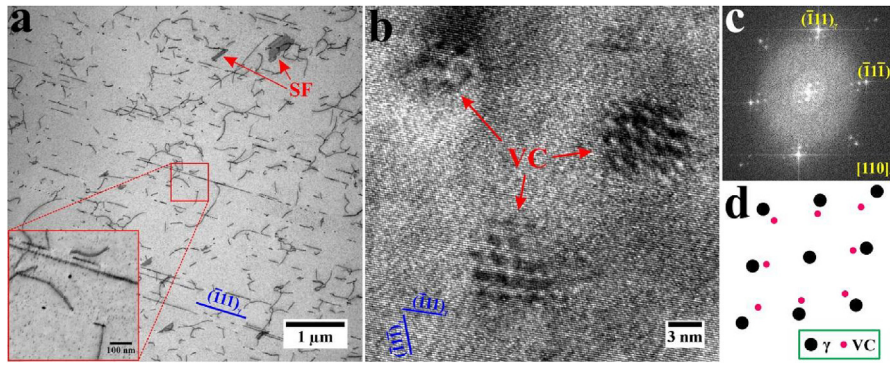
Fig. 2. Microstructures developed during aging at 650 °C for 2 h (a) STEM bright field image viewed along the $[110]_\gamma$ direction, where the red arrows point to stacking faults (SFs). (b) HRTEM image. (c) Fast Fourier transform pattern of (b). (d) Key diagram of (c). The blue lines indicate the edge-on $\{111\}_\gamma$ plane traces. (For interpretation of the references to color in this figure legend, the reader is referred to the Web version of this article.)
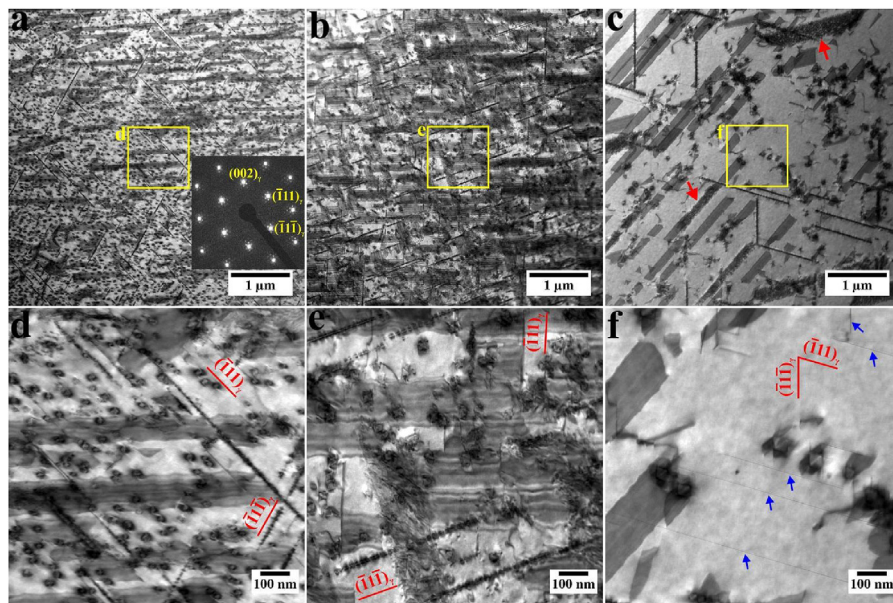

Fig. 3. STEM bright field images of the microstructures developed during aging at (a) 700 °C, (b) 750 °C and (c) 850 °C for 2 h (d–f) Images of the framed regions in (a), (b) and (c), respectively, taken at a higher magnification. All images are viewed along the $[110]_\gamma$ direction and the inset of (a) shows its corresponding SAD pattern. The red lines in (d–f) indicate the edge-on $\{111\}_\gamma$ plane traces. (For interpretation of the references to color in this figure legend, the reader is referred to the Web version of this article.)

patterns is illustrated in the inset of Fig. 3a, where additional satellite spots resulting from double diffraction [44] are also found close to the diffraction spots from γ and VC. Apart from the VC particles, a number of SFs rather than individual dislocations occur within the γ matrix (Fig. 3a–c). These SFs lie on the four sets of $\{111\}_\gamma$ planes, i.e., $(111)_\gamma$, $(11\bar{1})_\gamma$, $(\bar{1}11)_\gamma$ and $(\bar{1}1\bar{1})_\gamma$. Since the latter two sets of planes are parallel to the $[110]_\gamma$ direction, the corresponding SFs are viewed edge-on and hence appear as extremely thin straight lines as indicated by blue arrows in Fig. 3f. In terms of distribution, the precipitated VC particles can be categorized into two groups: (i) randomly distributed VC particles and (ii) bands of VC particles. The latter are formed on the SFs and have a smaller size as well as a higher number density than the former, as indicated by red arrows in Fig. 3c. Such bands of VC particles are found on all four sets of $\{111\}_\gamma$ planes, corresponding to the four variants of SFs. The edge-on bands lying on the sets of $(\bar{1}11)_\gamma$ and $(\bar{1}1\bar{1})_\gamma$ planes appear as coarse straight lines (straight strings of VC particles) as shown in Fig. 3a–f.

The increase of the VC particle size with increasing aging temperature is also revealed in Fig. 3. The randomly distributed VC particles precipitated during aging at 700 °C, 750 °C and 850 °C have an average size of 21 nm, 29 nm and 43 nm, respectively. For the former two aging temperatures, they sustain a uniform distribution within the γ matrix (Fig. 3a and b), while for the higher aging temperature, 850 °C, seem to have undergone Ostwald ripening, i.e., large particles growing at the expense of smaller particles, resulting in a non-uniform distribution and a lower particle number density (Fig. 3c). It should be noted that the number density of the SFs shown in Fig. 3c (850 °C) is also lower than that in Fig. 3a (700 °C) and b (750 °C).

The XRD analysis conducted on the sample aged at 750 °C (Supplementary Fig. S2) reveals that the lattice parameters of the γ matrix and the VC precipitate are $a_\gamma = 3.6069$ Å and $a_{VC} = 4.0978$ Å, respectively, i.e., the latter is 13.6% larger than the former. Such a lattice misfit is expected to cause accumulation of strain at the γ/VC interfaces with the growth of VC. Fig. 3d shows that most of the VC particles precipitated during aging at 700 °C are indeed surrounded by elastic strain contrast. On increasing the aging temperature to 750 °C, besides the occurrence of elastic strain contrast, the interfaces of some VC particles are associated with misfit dislocations,
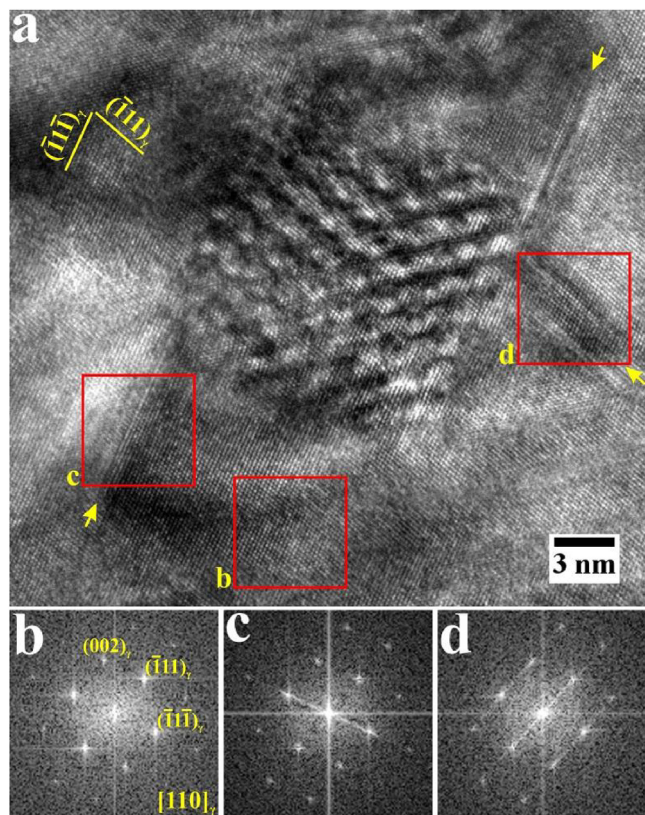
Fig. 4. HRTEM analysis of the VC precipitated during aging at 700 °C for 2 h: (a) HRTEM image; (b–d) Fast Fourier transform patterns of the framed regions in (a). The yellow lines indicate the edge-on $\{111\}_\gamma$ plane traces and the arrows point to the band contrast associated with the γ/VC interface. (For interpretation of the references to color in this figure legend, the reader is referred to the Web version of this article.)

Fig. 5. APT analysis of the VC particles precipitated during aging at 750 °C for 2 h (a, b) Reconstructed atom maps with VC particles visualized in terms of 20 at.% V iso-concentration surfaces. (c) Proximity histogram of the specific VC particle highlighted in magenta color in (a), showing the average concentration of various elements as a function of the distance from the γ/VC interface. (For interpretation of the references to color in this figure legend, the reader is referred to the Web version of this article.)

as illustrated in Fig. 3e. On further increasing the aging temperature to 850 °C, SFs occur surrounding the VC particles (Fig. 3f), which seem to result from the dissociation and extension of the dislocations emitted from the γ/VC interfaces. Closer observation by HRTEM reveals that the emission of SFs from the γ/VC interfaces also occurs for the former two aging temperatures (700 °C and 750 °C). An example is displayed in Fig. 4 for the sample aged at 700 °C. The HRTEM image of Fig. 4a shows a VC particle with strawberry-like contrast, where three bands (arrows) are found to be associated with the γ/VC interface, with two being parallel to the $(\bar{1}1\bar{1})_\gamma$ plane and the other one to the $(\bar{1}11)_\gamma$ plane. Compared to the FFT pattern for the region without band contrast (Fig. 4b), additional diffraction streaks along the $[\bar{1}1\bar{1}]^*_\gamma$ or the $[\bar{1}11]^*_\gamma$ direction are shown in the FFT patterns for the regions containing a band (Fig. 4c and d),[1] implying the existence of SFs within those bands.

Thermodynamic simulation shows that the VC precipitate primarily consists of V, C and Cr and its equilibrium composition exhibits only weak dependence on temperature (Supplementary Fig. S1). For analyzing the composition of the VC particles observed here, APT analysis was performed on the sample aged at 750 °C. Fig. 5a shows the reconstructed 3D atom map of a needle-shaped APT specimen, where the VC particles are visualized in terms of 20 at.% V iso-concentration surfaces. The enrichment of V and C atoms within these particles is clearly illustrated in the individual V and C atom maps (Fig. 5b). The proxigram (proximity histogram [45]) analysis for the specific VC particle highlighted in
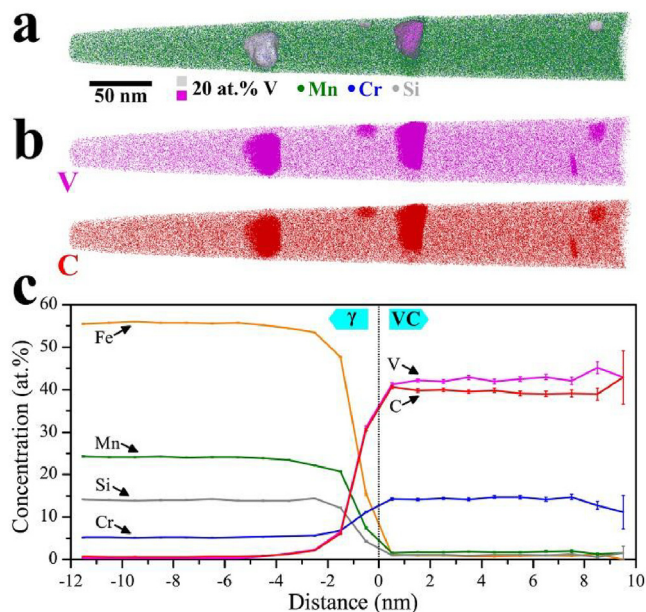
magenta color in Fig. 5a quantitatively reveals that the VC precipitate is also enriched with Cr, as displayed in Fig. 5c. This is consistent with the thermodynamic simulation. The average concentrations of V, C and Cr for that particle are 42.23 at.%, 39.63 at.% and 14.41 at.%, respectively. Considering that VC has a NaCl-type crystal structure, i.e., V-sites construct a fcc lattice in which C occupies the octahedral interstitial sites, the 14.41 at.% of Cr atoms should have occupied some of the V-sites and the ratio between (V, Cr) and C should be 1: 1 for an ideal crystal without any vacancy. By normalizing the measured concentrations to such a ratio and assuming that only interstitial vacancies are present, the chemical formula of the VC precipitate is estimated to be $(V_{0.75}Cr_{0.25})C_{0.70}$, where the missing 30 at.% of C atoms in the C-sublattice correspond to the vacancies.

3.3. Shape memory effect

In order to assess the SME (in terms of the recovery ratio) corresponding to the various pristine microstructures mentioned above, we first studied the recovery annealing temperature dependence of the recovery ratio using the samples aged at 750 °C. Those samples with a pre-strain of ~4% were subjected to recovery annealing at a series of temperatures and their recovery ratios were plotted in Fig. 6a. A considerable increase in the recovery ratio is revealed with increasing the recovery annealing temperature from 100 °C to 350 °C. On further increasing the temperature, however, this increase saturates, i.e., the recovery ratio remains almost constant for temperatures above 350 °C. This means that at such temperatures ($\geq$350 °C) the stress-induced ε martensite formed during pre-straining completely transforms into the parent γ austenite. In this study, to ensure the complete $\varepsilon \rightarrow \gamma$ transformation, all pre-strained samples were recovery annealed at 450 °C when assessing the SME.

Fig. 6b shows the recovery ratio as a function of pre-strain for both the as-solution treated and the aged states. A common

---

[1] The indices followed by an asterisk (*) refer to the reciprocal space in this paper.
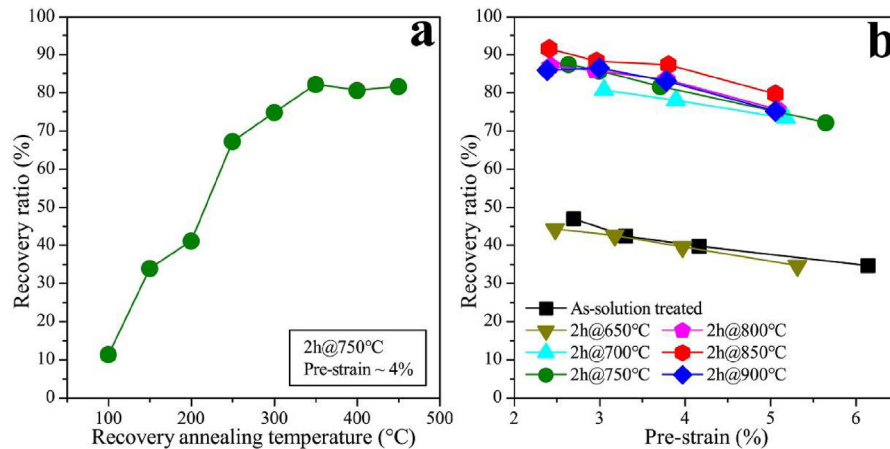
Fig. 6. (a) Recovery ratio as a function of recovery annealing temperature for the samples aged at 750 °C for 2 h, where a pre-strain of ~4% was applied and the holding time was 15 min for all recovery annealing temperatures. (b) Recovery ratio as a function of pre-strain for both the as-solution treated and the aged samples, where the recovery annealing was carried out at 450 °C for 15 min.

tendency for all of these states is that the recovery ratio decreases with the increase of pre-strain, which may be explained by the accumulation of irrecoverable strain resulting from slip deformation. The as-solution treated samples exhibit relatively low recovery ratios (<50%) for the entire pre-strain range (2.3–6.2%) investigated here, similar to most of the other as-solution treated polycrystalline Fe–Mn–Si-based shape memory alloys [13]. Aging at 650 °C is found to not improve the SME. Instead, it even results in somewhat lower recovery ratios, although a large number of small VC particles (~6 nm) as well as many dislocations have formed during the aging treatment (Fig. 2). When the aging temperature is raised to 700 °C, however, the recovery ratios exhibit an abrupt increase, reaching almost twice as high as those of the as-solution treated samples. On further increasing the aging temperature from 700 °C to 850 °C, the recovery ratios slightly increase further. For the samples aged at 850 °C, recovery ratios higher than 85% are reached for pre-strains $\leq$ 4%. Above 850 °C, however, a slight reduction in the recovery ratios is found, as revealed by the results of the samples aged at 900 °C. From correlating the SME with the pristine microstructures, we conclude that the remarkable improvement of SME by aging is associated with the formation of (i) large VC particles ($\geq$21 nm) and (ii) a number of SFs. To clarify the underlying role of these two factors in improving the SME, we compare in the following the evolution of stress-induced ε martensite plates with increasing applied strain and the characteristics of these plates between the as-solution treated and the high-temperature aged samples (with aging temperature $\geq$ 700 °C).

3.4. Stress-induced martensite

Fig. 7 shows the results of an in situ three-point bending experiment, where the evolution of stress-induced ε martensite plates (visualized as bright bands) with increasing applied strain in the as-solution treated sample is illustrated. It should be emphasized that most of the martensite plates were nucleated from grain boundaries, as revealed in the inset of Fig. 7a. The initially formed martensite plates were relatively thin (~50 nm) as shown in Fig. 7a, where the two arrows point to the ends of two individual martensite plates lying on the same $\{111\}_\gamma$ plane. On increasing the

applied strain, as seen in Fig. 7b, these two plates coalesced into one single plate. On further increasing the applied strain (Fig. 7c–f), more martensite plates formed and some plates thickened via lateral growth along their transverse direction. In Fig. 7f, three bands designated as A, B and C are indicated by three pairs of parallel dashed lines. The rather thick band A and band C are developed from the thickening and coalescence of two closely spaced plates, as indicated by arrows in Fig. 7d and e, respectively. It can be noted that, with the increase of the applied strain from Fig. 7c–f, only the plates included in band A and band C thickened, while the thickness of the plates between these two bands remained almost unchanged. This means that these two groups of martensite plates may lie on two different sets of $\{111\}_\gamma$ planes, i.e., they are nonparallel relative to each other, although their intersections with the surface (plane traces) appear almost parallel to each other. Such a hypothesis is justified by the EBSD plane trace analysis illustrated at the top of Fig. 7, which reveals that the traces of the $(\bar{1}11)_\gamma$ and $(\bar{1}1\bar{1})_\gamma$ planes look almost parallel relative to each other (~1° deviation).

For examining the internal microstructures of the stress-induced ε martensite plates, a through-thickness TEM lamella was prepared from the location indicated by a rectangle in Fig. 7f. The overview of the lamella is displayed in Fig. 8a, where the cross sections of the three bands, A, B and C, are shown. It is confirmed that band A and band C are parallel to each other, i.e., lying on the same set of $\{111\}_\gamma$ planes, but they are nonparallel to band B as well as other martensite plates (more clearly seen in Fig. 8b) located between them. Fig. 8b and c show that both band A and band C consist of two separated thick plates, implying that the pairs of closely spaced plates (indicated by arrows in Fig. 7d and e) included in these two bands were not merged together. Within the individual thick plates (hundreds of nanometers thick), a number of straight line features can be seen, which appear like edge-on SFs. The SAD pattern (Fig. 8d) taken around the γ/ε interface and its key diagram (Fig. 8e) reveal that the orientation relationship between the γ matrix and the ε martensite is $(1\bar{1}1)_\gamma//(0001)_\varepsilon$ and $[110]_\gamma//[2\bar{1}\bar{1}0]_\varepsilon$. The SAD pattern also shows streaks along the $[0001]_\varepsilon^*$ direction, demonstrating the existence of SFs within the martensite plates. Fig. 8f shows the dark field image of band C taken using the $(01\bar{1}0)_\varepsilon$ diffraction spot, where a number of straight dark lines parallel to the $(0001)_\varepsilon$ plane are illustrated within the two bright martensite plates. These dark lines should correspond to the line features seen in the bright field image (Fig. 8c). Indeed, they are also

---

[2] The length of the red lines is proportional to the angle between the corresponding $\{111\}_\gamma$ plane and the surface.
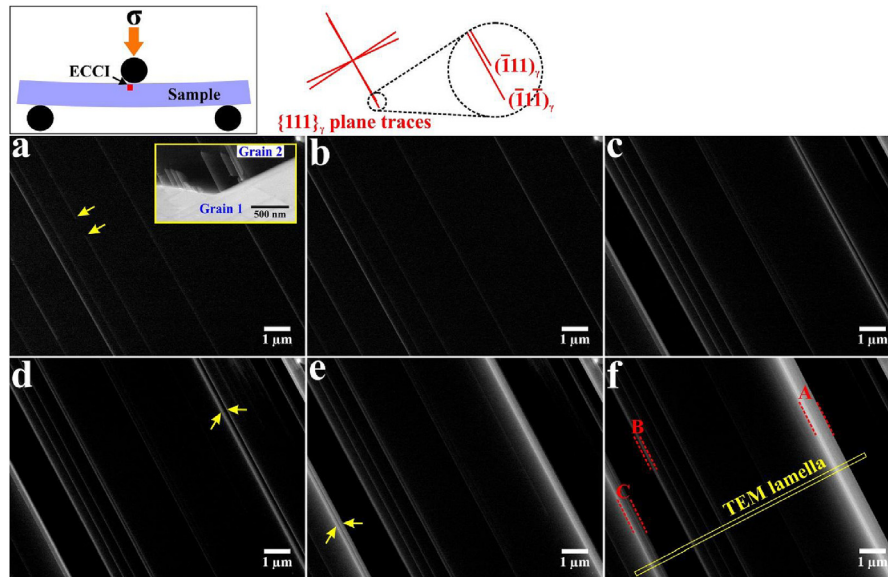
Fig. 7. ECCI observation of the evolution of stress-induced ε martensite plates in the as-solution treated sample. (a–f) Sequential images taken from the same region on a pre-polished flat specimen subjected to in situ three-point bending. The bending process and the {111}$_\gamma$ plane traces (red lines) determined by EBSD are schematically illustrated on top of these images.[2] The inset of (a) shows the nucleation of martensite plates from a grain boundary. The applied strain was consecutively increased from (a) to (f). (For interpretation of the references to color in this figure legend, the reader is referred to the Web version of this article.)
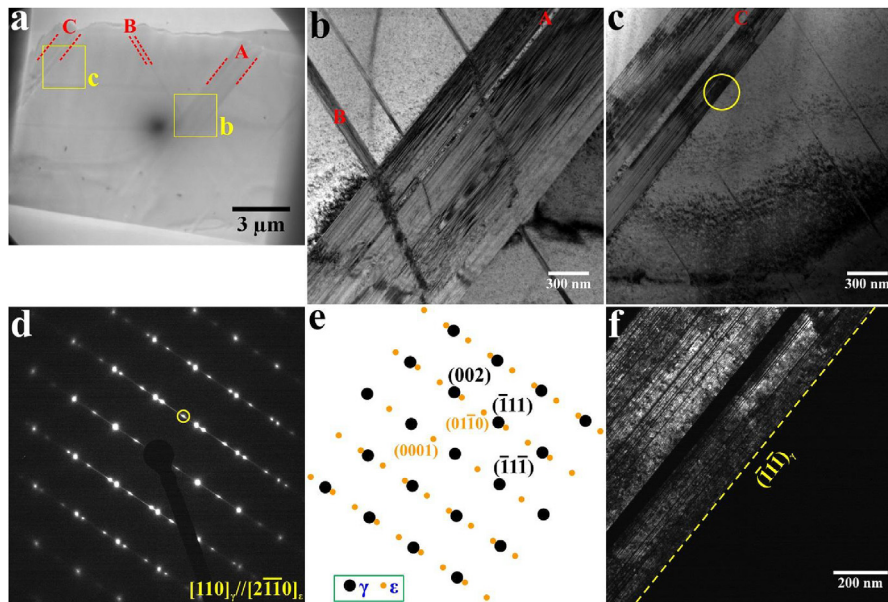

Fig. 8. TEM analysis of the lamella lifted out from the location indicated by a rectangle in Fig. 7f. (a) Low magnification overview of the FIB lift-out lamella. (b, c) Bright field images of the framed regions in (a) taken at a higher magnification. (d) $[110]_\gamma//[2\overline{1}\overline{1}0]_\varepsilon$ SAD pattern of the circled area in (c). (e) Key diagram of (d). (f) Dark field image taken using the circled diffraction spot in (d).

visible in the corresponding HRTEM image, as indicated by arrows in Fig. 9a. This HRTEM image is viewed along the $[110]_\gamma//[2\overline{1}\overline{1}0]_\varepsilon$ direction, as identified by the FFT patterns displayed in Fig. 9b–d. Comparing the FFT patterns for the regions without and with the line features (Fig. 9c and d), additional streaks along the $[0001]_\varepsilon^*$ direction are observed in the latter, demonstrating that those lines are indeed edge-on SFs lying on the set of $(0001)_\varepsilon$ planes.

It is expected that the presence of additional VC particles and SFs in the high-temperature aged samples (with aging temperature $\geq$ 700 °C and improved SME) would render the stress-induced ε martensite plates evolve in a manner different from that of the as-

solution treated sample. Taking the sample aged at 700 °C as a reference example, the formation process of the martensite plates with increasing applied strain is shown in Fig. 10, where the sequential images (Fig. 10a–d) were also taken from an in situ three-point bending experiment. Fig. 10a shows the initial microstructure, in which the uniformly distributed VC particles and two variants of SFs lying on the sets of $(11\overline{1})_\gamma$ and $(111)_\gamma$ planes are clearly illustrated. The VC particles appear as bright dots and the SFs bright straight lines on one side and fading contrast on the other side. The other two variants of SFs are nearly parallel to the incident beam and exhibit weak contrast. With the application of
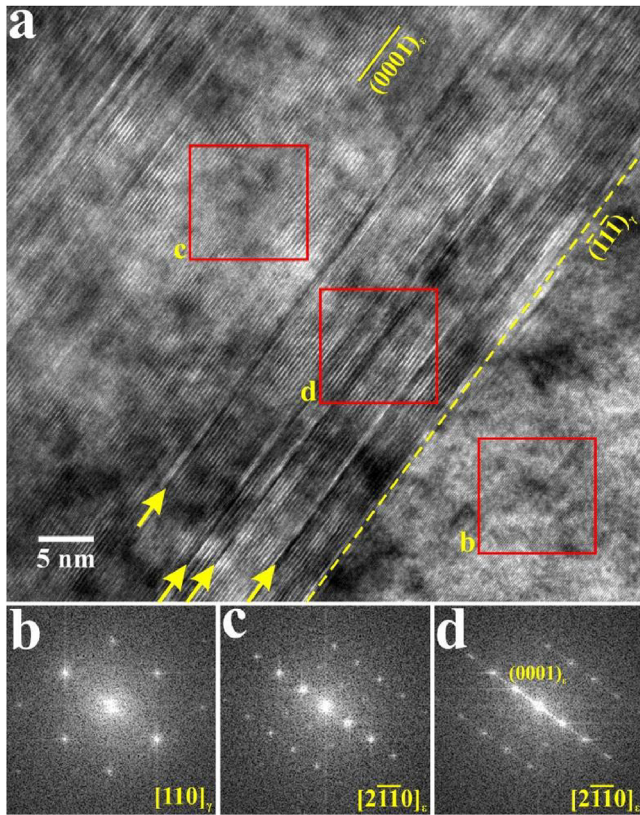
Fig. 9. HRTEM analysis of an area surrounding the γ/ε interface indicated by a dashed line in Fig. 8f: (a) HRTEM image; (b–d) Fast Fourier transform patterns of the framed regions in (a).

an external strain (Fig. 10b), more SFs on the set of $(111)_\gamma$ planes formed and a few of the pre-existing SFs on this set of planes extended. Such processes continued with the increase of the applied strain, as shown in Fig. 10c and d. It should be noted that most of the SFs generated during straining seem to nucleate from the VC particles. The accumulation and extension of SFs on the same plane lead to the coalescence of individual SFs, generating longer SFs. Fig. 10c and d also reveal that such long SFs tend to be spaced regularly with the increase of the applied strain. When the spacing between adjacent long SFs reaches $2d_{\{111\}}$ (twice the spacing between adjacent $\{111\}_\gamma$ planes), the local regions will collapse into ε martensite [46]. However, such a small spacing ($2d_{\{111\}} = 4.17$ Å) is beyond the spatial resolution limit of ECCI. Detailed characterization of the stress-induced ε martensite in the high-temperature aged samples by TEM is presented below in Fig. 11 and Fig. 12.

Fig. 10 also shows that the other variant of SFs lying on the set of $(11\bar{1})_\gamma$ planes behaved quite differently. On applying an external strain (from Fig. 10a to b), a few of the pre-existing SFs underwent shrinkage such as the one indicated by a green arrow in Fig. 10a. On increasing the applied strain (from Fig. 10b to c), some pre-existing SFs as indicated by red arrows in Fig. 10b disappeared. At a higher strain level (Fig. 10d), more pre-existing SFs disappeared, but it was also found that several new SFs were generated on the set of $(11\bar{1})_\gamma$ planes. It should be emphasized that the remaining pre-existing SFs and the newly formed SFs still exhibit relatively random distribution, i.e., they do not tend to form the ε martensite. Thus, only one martensite variant (on the set of $(111)_\gamma$ planes) is expected to form within the field of view.

Wider-area TEM observation was performed on the TEM foils

prepared by conventional twin-jet electropolishing to compare the stress-induced ε martensite plates between the as-solution treated and the high-temperature aged samples. As shown in Fig. 11a and b, under the same amount of tensile strain (4%), the martensite plates formed in the as-solution treated sample exhibit a lower number density and a larger thickness (95 nm on average) than those in the aged sample. Another difference revealed is that the martensite plates in the as-solution treated sample have multiple variants lying on different sets of $\{111\}_\gamma$ planes (Fig. 11a and also Fig. 8a), while those in the aged sample belong to the same variant (Fig. 11b). Indeed, the larger-scale SEM observation (Supplementary Fig. S3) illustrates that the martensite plates in each grain of the aged sample exhibit a single variant and they are uniformly distributed. We also find that the yield stress $\sigma_{0.2}$ of the as-solution treated sample and of the sample aged at 850 °C is 320 MPa and 410 MPa, respectively, either of which is lower than the corresponding applied stress displayed in Fig. 10a and b, i.e., dislocation slip has already been activated in both samples. This is consistent with the occurrence of entangled dislocations in Fig. 11a.

In Fig. 11b, the VC particles are shown to be either randomly distributed or located within a band, identical to that revealed in Fig. 3. The average size of the VC particles within the bands was estimated to be 15 nm, which is smaller than that of the randomly distributed ones (43 nm). Fig. 11c and d illustrate the two framed regions in Fig. 11b at higher magnifications, where the former corresponds to the randomly distributed VC particles and the latter to the bands of VC particles. It is shown that both types of VC particles have not prevented the propagation of the martensite plates, i.e., the tips of the martensite plates have practically cut through the VC particles and propagated further. This phenomenon is even more clearly revealed by the HRTEM analysis, as shown in Fig. 12. The strawberry-like contrast indicated by ellipses in Fig. 12a and b are VC particles as demonstrated in Subsection 3.2. The ε martensite plates appear as band contrast within the γ matrix, as identified by the inset FFT pattern in Fig. 12a, and their thickness ranges from several layers of $\{0001\}_\varepsilon$ lattice spacing to ~3 nm. The penetration of the martensite plates through the VC particles is clearly seen in both Fig. 12a and b, verifying that the VC particles cannot prevent the propagation of the martensite plates.

4. Discussion

In the present study, an as-solution treated Fe–28Mn–6Si–5Cr–0.764V–0.18C alloy was subjected to aging treatment at various temperatures (650–900 °C) for precipitating VC particles. TEM microstructural characterization shows that VC particles are not the only product of aging. Depending on the holding temperature, dislocations and SFs are formed as well during aging. On the basis of the aging products and their respective influence on the SME with respect to the as-solution treated reference state, we identify two categories of aged states. The first category (650 °C) is associated with the formation of rather small VC particles (~6 nm) and profuse dislocations ($2.26 \pm 0.098 \times 10^{13}$ m^{-2}) during aging (Fig. 2). These products slightly reduce the recovery ratio (Fig. 6), implying that the VC precipitation does not necessarily improve the SME. The second category ($\geq$700 °C) involves the formation of larger VC particles ($\geq$21 nm) and a number of SFs during aging (Fig. 3). Remarkable improvement of the SME is observed in this category (Fig. 6). The results of in situ SEM three-point bending experiments (Fig. 10) and TEM microstructural characterization (Figs. 11 and 12) reveal two main facts: (i) the VC particles do not act as nucleation sites of the stress-induced martensite plates; and (ii) the proceeding martensite plates can cut through the VC particles. These two facts are contrary to the previous speculations on the role of the carbide and nitride precipitates in improving the SME [21,22,24–27,39,40].
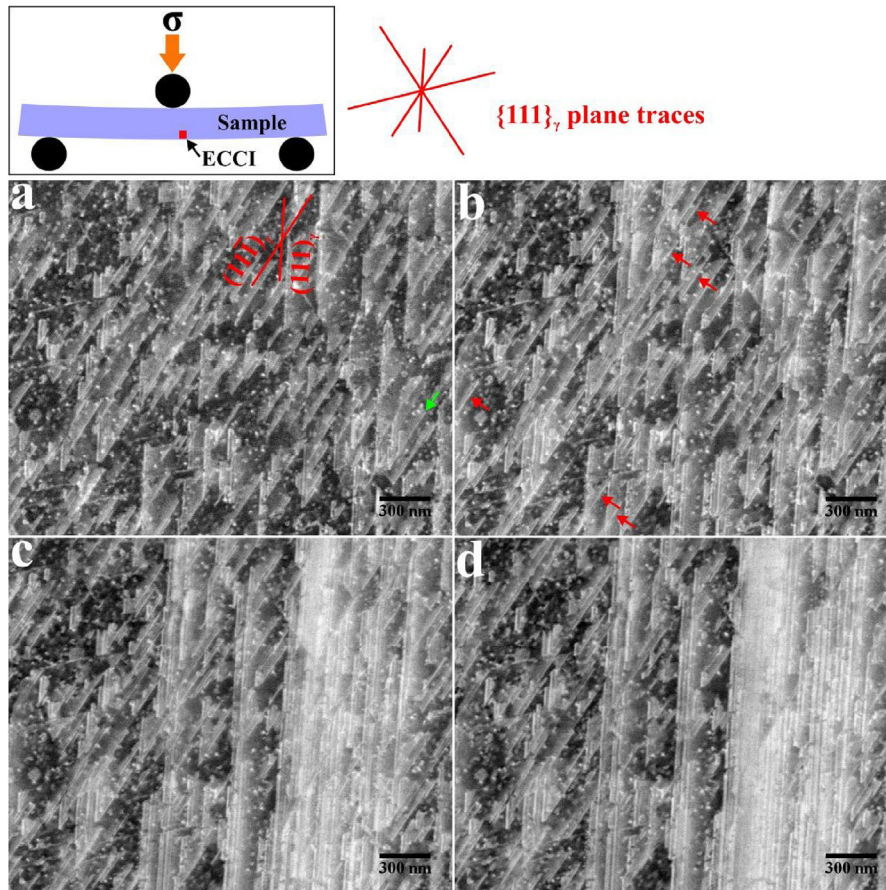
Fig. 10. ECCI observation of the formation of stress-induced ε martensite plates in the sample aged at 700 °C for 2 h (a—d) Sequential images taken from the same region on a pre-polished flat specimen subjected to in situ three-point bending. The bending process and the {111}$_\gamma$ plane traces (red lines) determined by EBSD are schematically illustrated on top of these images. The applied strain was consecutively increased from (a) to (d). (For interpretation of the references to color in this figure legend, the reader is referred to the Web version of this article.)
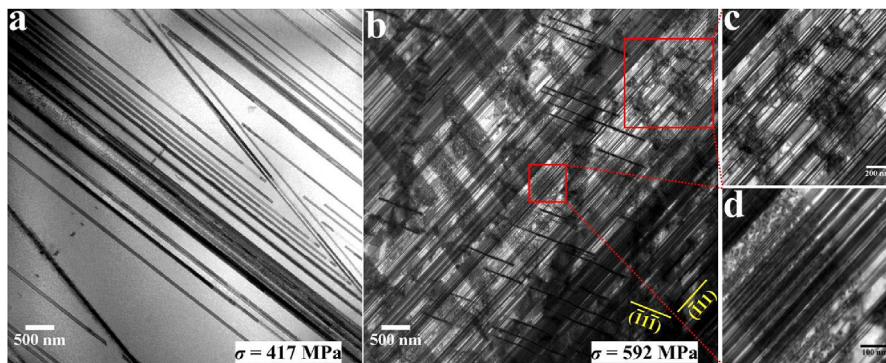

Fig. 11. STEM bright field images of the stress-induced ε martensite plates in (a) the as-solution treated sample and (b—d) the sample aged at 850 °C for 2 h. Tensile deformation to the same amount of strain (4%) was applied to induce the formation of martensite plates for both samples. The corresponding tensile stresses at this strain level are displayed in (a) and (b) as well.

On the other hand, the SFs that are generated during aging have been revealed to play an important role in the $\gamma \rightarrow \varepsilon$ martensitic transformation, leading to the formation of very thin (<3 nm) single-variant martensite plates within each grain. Below we discuss the formation of SFs during aging and the reasons for the improvement of SME in the high-temperature aged samples (i.e., the second category of aged states with aging temperature ≥ 700 °C).

4.1. Occurrence of stacking faults accompanying the precipitation of VC

The occurrence of SFs accompanying particle precipitation has also been reported in bulk dislocation-free Si [47] and Fe—Cr—Ni-based austenitic stainless steels [48—53]. In both cases, excess dislocations were generated as a result of local lattice distortion at
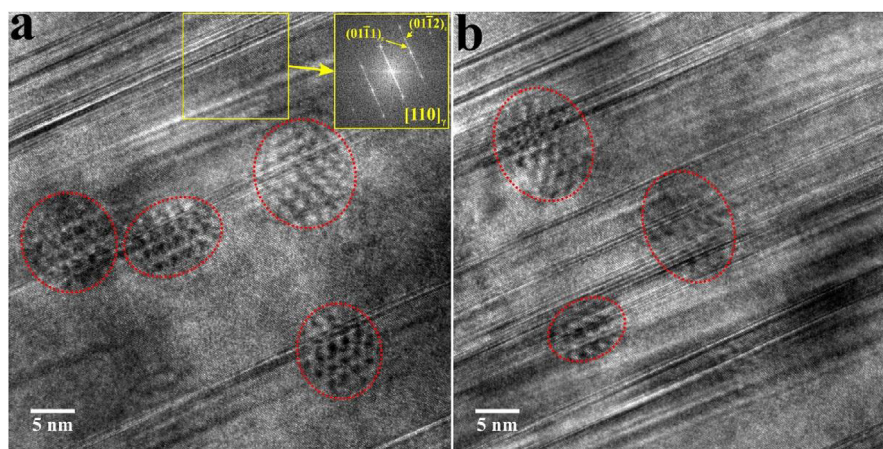
Fig. 12. HRTEM analysis of the interaction between stress-induced ε martensite plates and VC particles in the sample aged at 850 °C for 2 h. The red ellipses indicate the positions of VC particles which are characterized by strawberry-like contrast. (For interpretation of the references to color in this figure legend, the reader is referred to the Web version of this article.)

the particle/matrix interface. In bulk dislocation-free Si, the SFs, generated during oxide precipitation at high temperatures, have been revealed to nucleate either by (i) the collapse of interstitial Si atoms at the particle/matrix interface or by (ii) the dissociation of the dislocations associated with the particle/matrix interface. Resembling what we have observed in the present Fe−Mn−Si-based alloy, the as-solution treated Fe−Cr−Ni-based austenitic stainless steels were found to contain few SFs and a relatively low concentration of dislocations [50]. After aging, SFs occurred in these stainless steels accompanying the precipitation of carbide particles, including NbC [48−50,53], TiC [50], VC [51] and TaC [52]. In these pioneering studies, however, all SFs were regarded as being decorated by densely distributed carbide particles, i.e., all of them were considered to be bands of carbide particles.[3] Based on this argument, two similar mechanisms were proposed by Silcock et al. [49] and Van Aswegen et al. [50], respectively, to account for the growth of the SFs. These two mechanisms assumed that the SFs nucleated via the dissociation of $1/2<110>_\gamma$ dislocations, while the nucleation and growth of the carbide particles at the leading partial dislocations caused the leading partials to move further, i.e., extending the SFs. Apparently, in both dislocation-free Si and Fe−Cr−Ni-based austenitic stainless steels, the dislocations generated at the particle/matrix interface are important sources of the SFs.

In the present Fe−Mn−Si-based alloy, the critical size of the VC particles for generating geometrically necessary interface dislocations is estimated to be 2.9 nm based on the fact that the lattice parameter of the VC precipitate is 13.6% larger than that of the γ matrix [54]. This can explain the occurrence of profuse dislocations in the sample aged at 650 °C (Fig. 2a), where the average size of the VC particles already reaches ~6 nm. However, very few of the dislocations dissociate to form SFs at this temperature. Only at higher aging temperatures (700 and 750 °C), a number of SFs occur (Fig. 3a and b). This is in contrast to the generally observed trend that stacking fault energy (SFE) increases with temperature. A possible reason for this inconsistency would be that more solute atoms segregate to the newly generated dislocations during high-temperature aging, resulting in the local lowering of the SFE at the dislocations [55,56] and thus causing the dislocations to

dissociate to nucleate SFs. In this context, the almost complete absence of SFs in the samples aged at low temperatures (≤650 °C) can be explained by the lower solute concentrations at the dislocations, which result from the lower diffusivity of alloying elements at low temperatures. Once a SF has been nucleated at high temperatures, its growth can also proceed by the further segregation of solute atoms to it, a phenomenon referred to as Suzuki effect [57]. This effect reduces the local SFE and thus causes the SF to extend further. Since not all of the SFs are decorated by densely distributed VC particles and even the SFs not in association with any VC particle are also present (Fig. 3), we conclude that the two mechanisms proposed for the growth of SFs in Fe−Cr−Ni-based austenitic stainless steels [49,50] do not apply in the present alloy.

Considering that all aged samples were water quenched to room temperature, the fast cooling rate (>100 °C/s [58]) is expected to suppress all microstructural changes which are associated with long-range diffusion upon cooling. The linear coefficient of thermal expansion (CTE) for the VC precipitate and the γ matrix is roughly 7.7×10^{-6} /°C and 16×10^{-6} /°C, respectively [59,60]. Given that the average size of the VC particles in the samples aged at 650−850 °C is 6−43 nm, the strain caused by the difference of the CTE between VC and γ upon cooling is calculated to be 0.5−0.7%. It is reasonable to expect that such a small strain can be accommodated by the elastic deformation of the local VC precipitate and its surrounding γ matrix. Thus, no significant microstructural change is expected to occur during cooling.

The experimental results also show that the number density of the SFs decreases in the samples aged at relatively high temperatures (≥850 °C). A similar phenomenon was also observed in Fe−Cr−Ni-based austenitic stainless steels [50], where the reduced number density was ascribed to the instability of the SFs upon tempering at very high temperatures. It was proposed that some SFs were removed by reverse movement of the original partial dislocations or by action of newly generated partial dislocations [50]. Such a scenario is, however, not yet justified by direct experimental evidence. Further research is required to clarify it as well as the question which solutes are responsible for lowering the local SFE.

---

[3] A close examination of the images attained over 60 years ago in the pioneering studies [48−52] shows that stacking faults which are not decorated by densely distributed carbide particles are indeed present as well, especially at the early stages of aging.

4.2. Reasons for the improvement of the shape memory effect

As is well shown, the stress-induced martensitic transformation from fcc γ to hcp ε is kinetically accomplished by slip of $1/6<11\bar{2}>_\gamma$

Shockley partial dislocations or equivalently introduction of SFs on every second layer of the $\{111\}_\gamma$ planes. This process changes the stacking sequence of the close-packed planes from ABCABCAB into ABABABAB (Fig. 13). On each $\{111\}_\gamma$ plane, the Shockley partials have three possible Burgers vectors, e.g., $1/6[11\bar{2}]_\gamma$, $1/6[1\bar{2}1]_\gamma$ and $1/6[\bar{2}11]_\gamma$ on the $(111)_\gamma$ plane (b_1, b_2 and b_3 shown in Fig. 13a). Due to the threefold rotational symmetry about the $\langle111\rangle$ axis of the fcc crystal, the slip of any one of the three different partials results in the same change in the stacking sequence for the block above the slip plane, i.e., C → A, A → B and B → C. This means that the resultant ε martensite has the same orientation relationship with the γ matrix, no matter which partials (on the same set of $\{111\}_\gamma$ planes) participate in the martensitic transformation. For instance, the same 8-layer martensite (ABABABAB stacking) can be produced not only by the slip of three different partials (b_1, b_2 and b_3, Fig. 13b) but also by the slip of three identical partials (b_1, Fig. 13d and e). However, the macroscopic strain s produced by the $\gamma \to \varepsilon$ martensitic transformation is determined by the Burgers vectors of the participating Shockley partials. When the transformation is accomplished by slip of an equal number, say, n, of the three different partials (Fig. 13b), zero net macroscopic strain is produced, since $nb_1 + nb_2 + nb_3 = 0$. This case is expected to occur in the thermally induced martensitic transformation. For the stress-induced martensitic transformation, most of the participating partials are expected to have the same Burgers vector considering that the partials with a larger Schmid factor are preferentially activated under a specific external and locally resolved stress field. Fig. 13d schematically illustrates that the maximum transformation strain $s_{max} = 0.3536$ can be attained when the ε martensite is formed by the partials with the same Burgers vector. Such kind of martensite has been termed as mono-partial martensite by Bergeon et al. [61,62]. We will use this terminology in the following discussion. It should be noted that a smaller transformation strain $(0 \leq s < 0.3536)$ will be produced if the participating partials are not

of the same Burgers vector.

In polycrystalline Fe–Mn–Si-based alloys, previous atomic force microscopy (AFM) studies [28,34,36,38] have revealed that most of the individual stress-induced ε martensite plates are actually mono-partial martensite, but various martensite variants on different $\{111\}_\gamma$ planes may occur within the same grain. In such a case, the strains produced by different martensite variants cancel each other out to some extent, leading to a reduced overall strain. Thus, the formation of a single variant within each grain is important for obtaining a large transformation strain in polycrystalline alloys. In the present Fe–Mn–Si-based alloy, the deformation microstructures reveal that the pre-strain ε_p is produced not only by stress-induced martensitic transformation but also by dislocation slip, i.e., ε_p consists of two components. Since only the transformation strain can potentially be recovered under thermal activation, the fraction of this component should be as large as possible for obtaining a large recovery strain. This indicates that the formation of a single martensite variant within each grain (Fig. 11b and Supplementary Fig. S3) is one of the reasons for the improvement of SME in the high-temperature aged samples. For the as-solution treated sample, the coexistence of multiple martensite variants (Figs. 8 and 11a) implies that its transformation strain is lower than that of the aged samples for a given ε_p, i.e., more dislocation activity is involved in the as-solution treated sample.

During recovery annealing, the reverse martensitic transformation from ε to γ is also kinetically accomplished by slip of $1/3<0\bar{1}10>_\varepsilon$ partial dislocations (i.e., introduction of SFs) on every second layer of the $\{0001\}_\varepsilon$ planes. There are also three possible Burgers vectors for the partials on each $\{0001\}_\varepsilon$ plane, e.g., $1/3[0\bar{1}10]_\varepsilon$, $1/3[\bar{1}100]_\varepsilon$ and $1/3[10\bar{1}0]_\varepsilon$ on the $(0001)_\varepsilon$ plane ($b_{1'}$, $b_{2'}$ and $b_{3'}$ shown in Fig. 13c). The orientation relationship between γ and ε guarantees that the three Burgers vectors of the partials on each $\{0001\}_\varepsilon$ plane are antiparallel to those of the Shockley partials on the corresponding $\{111\}_\gamma$ plane, as illustrated in Fig. 13c. This means
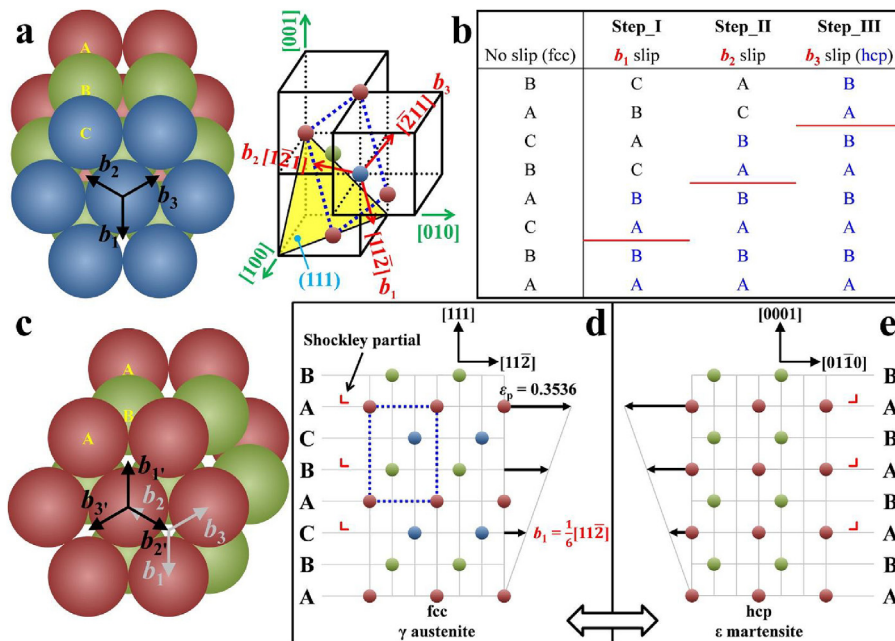

No slip (fcc)	Step_I b_1 slip	Step_II b_2 slip	Step_III b_3 slip (hcp)
B	C	A	B
A	B	C	A
C	A	B	B
B	C	A	A
A	B	B	B
C	A	A	A
B	B	B	B
A	A	A	A

Fig. 13. Schematic illustration of the transformation between fcc γ and hcp ε. (a) Characteristic ABCABCAB stacking in the γ crystal. b_1, b_2 and b_3 are Burgers vectors of the three Shockley partials on the $(111)_\gamma$ plane. (b) Evolution of the stacking sequence during the $\gamma \to \varepsilon$ transformation via the slip of three different Shockley partials on every second layer of the $\{111\}_\gamma$ planes. (c) Characteristic ABABABAB stacking in the ε crystal. $b_{1'}$, $b_{2'}$ and $b_{3'}$ are Burgers vectors of the three partials on the $(0001)_\varepsilon$ plane which are antiparallel to those of the Shockley partials. (d) Forward $\gamma \to \varepsilon$ and (e) backward $\varepsilon \to \gamma$ transformations via the slip of mono-partial dislocations (with the same Burgers vector) on every second layer of their close-packed planes.

that a partial residing at the martensite tip will have antiparallel Burgers vectors when moving within the γ matrix and within the ε martensite, respectively, as shown in Fig. 14. On straining it moves within the γ matrix to extend the martensite (martensitic transformation) and produces a transformation strain, while on recovery annealing it will move back towards the martensite interior (reverse martensitic transformation) driven by the Gibbs energy difference $\Delta G^{\varepsilon \to \gamma}$ and will thus completely remove the transformation strain (see also Fig. 13e). Therefore, a perfect SME (recovery ratio = 100%) can be attained as long as the reverse martensitic transformation is accomplished by the partials residing at the martensite tip, i.e., the partials that have participated in the $\gamma \to \varepsilon$ martensitic transformation. In polycrystalline Fe−Mn−Si-based alloys, however, the ε martensite tips frequently interact with obstacles such as dislocations, precipitates, α' martensite, grain boundaries, annealing twin boundaries and other variants of ε martensite, which may result in the annihilation of the partials at the martensite tips or trap them. In such cases, new partials have to be nucleated under thermal activation to accomplish the reverse martensitic transformation and the Burgers vectors of these new partials can principally be randomly aligned. This means that the Burgers vectors of the newly generated partials will most likely not be antiparallel to those of their counterparts participating in the martensitic transformation, leading to a reduced recovery strain. Such a situation has been identified by previous AFM studies [34,36] in the circumstances that the martensite tips reach the free surface, where the leading partials escaped out of the free surface and new partials were generated to mediate the reverse martensitic transformation, causing incomplete recovery of the strain. Thus, it is essential to retain the partials residing at the martensite tips and ensure their activity during recovery annealing for obtaining a large recovery strain in polycrystalline Fe−Mn−Si-based alloys.

For the present Fe−Mn−Si-based alloy, most of the martensite plates that are formed in the as-solution treated sample are fairly thick (from tens to hundreds of nanometers) and their different variants intersect with each other (Figs. 8 and 11a). α' martensite is expected to occur at the intersection sites as reported in similar Fe−Mn−Si-based alloys [28,63] and this phase is supposed to reduce the recovery strain by blocking reverse movement of the

partials during recovery annealing. From this point of view, we can also conclude that the formation of a single variant within each grain is beneficial for attaining better SME. Kajiwara [33] claimed that during deformation the tips of fairly thick martensite plates could not stop moving before reaching grain boundaries due to the large strain fields built up around the advancing tips. As a result, most of the partials residing at the thick martensite tips inevitably interact with the grain boundaries. In such a case, some of the partials may be trapped by the grain boundaries [64], so that they cannot move under thermal activation. The current alloy contains numerous annealing twin boundaries ($L_{TB}/L_{GB+TB} = 47.81\%$, Fig. 1a) as well, which also interact with the partials at the tips of the thick martensite plates [65]. It should be noted that incoherent annealing twin boundaries contain a series of Shockley partials [66], which could annihilate the approaching partials at the martensite tips when their Burgers vectors are opposite to each other. This indicates that incoherent twin boundaries are generally more effective in reducing the recovery strain than grain boundaries. Recently, Wen et al. [32] reported that the recovery strain could be significantly increased (up to 7.6%) by suppressing the formation of annealing twin boundaries in Fe−Mn−Si-based alloys. Such a phenomenon is consistent with the critical role of the incoherent twin boundaries in reducing the recovery strain. Thus, (i) the intersection between different martensite variants and (ii) the inevitable interaction between the thick martensite plates and the grain boundaries as well as annealing twin boundaries render it difficult to obtain a large recovery strain for the as-solution treated sample.

For the high-temperature aged samples, the martensite plates are very thin (from several layers of $\{0001\}_\varepsilon$ lattice spacing to ~3 nm), corresponding to rather small strain fields around their tips. It is supposed that such small strain fields can be accommodated by the matrix ahead of the martensite tips [33,34,36], i.e., the partials residing at the martensite tips are expected to be retained in the grain interior. On the other hand, TEM observations reveal that the martensite tips can cut through the VC particles in the aged samples (Fig. 11b–d and Fig. 12), i.e., the partials residing at the martensite tips can move through the VC particles. This means that the reverse martensitic transformation in those aged samples can proceed via the reverse movement of the partials retained within the grain, leading to a large recovery strain. Thus, the formation of very thin martensite plates is another reason for the improvement of SME in the high-temperature aged samples.

The formation of single-variant and extremely thin (~1 nm) stress-induced martensite plates was also typically observed in trained Fe−Mn−Si-based alloys [33−37,67], where the high densities of SFs produced by training were considered to be indispensable for the formation of this type of martensite plates [33,36,37]. The present high-temperature aged samples also contain a number of SFs (Fig. 3) before being subjected to deformation. Fig. 10 shows their critical role in the formation of the martensite plates: the stress-induced martensitic transformation proceeds by accumulation and regular arrangement of the long SFs, which are formed by a combination of the pre-existing SFs and the newly nucleated SFs on a specific set of $\{111\}_\gamma$ planes. Some of the pre-existing SFs, thus, become a portion of the martensite plates, lowering the energy required for the martensitic transformation. This implies that the critical resolved shear stress (CRSS) for the martensitic transformation in these aged samples is lower than that in the as-solution treated sample (without pre-existing SFs). Indeed, the decrease of the CRSS with the precipitation of VC was also observed in an Fe−17Mn−5Si−10Cr−4Ni(−1VC) alloy [68]. In the as-solution treated sample, the martensite variant selection may be not governed by the maximum Schmid factor, i.e., at the high stress level for activating martensitic transformation the
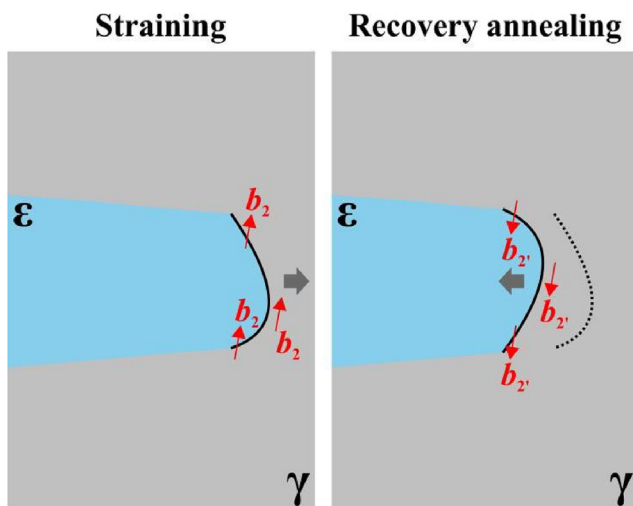

Fig. 14. An example of the movement of a partial dislocation residing at the ε martensite tip. On straining it moves within the γ matrix to extend the martensite further, so its Burgers vector is determined with respect to the fcc crystal, say, $\boldsymbol{b_2} = 1/6[1\bar{2}1]_\gamma$. During recovery annealing it moves within the martensite to shrink it. Its Burgers vector is thus determined with respect to the hcp crystal, which would be $\boldsymbol{b_{2'}} = 1/3[\bar{1}100]_\varepsilon$, i.e., antiparallel to $\boldsymbol{b_2}$.

martensite variants with somewhat lower Schmid factors may be nucleated as well, resulting in the formation of multiple martensite variants within each grain. On the contrary, it can be inferred that only the variant with the maximum Schmid factor occurs in the high-temperature aged samples due to their low CRSS. By assuming that each martensite plate nucleates on a pre-existing SF, Kajiwara [33] proposed a mechanism to explain why the martensite plates are extremely thin in trained Fe–Mn–Si-based alloys. However, such an assumption cannot be justified by our in-situ straining experiments (Fig. 10). Further research is required to clarify this issue.

5. Conclusions

The precipitation of VC during aging and its influence on the shape memory effect have been investigated in an Fe–28Mn–6Si–5Cr–0.764V–0.18C shape memory alloy. To explore the origin for the improvement of the shape memory effect by precipitating VC, detailed TEM characterization was carried out to analyze the microstructures of the stress-induced ε martensite plates and in situ ECCI observation was performed to examine the evolution of these plates during straining. Based on the experimental observations, we draw the following conclusions:

- The as-solution treated alloy consists of a single γ phase and contains few stacking faults. Aging at 650 °C produces profuse dislocations ($2.26 \pm 0.098 \times 10^{13}\,\mathrm{m^{-2}}$) and homogeneously distributed VC particles, which have an average size of 6 nm. When aging at higher temperatures (700–900 °C), larger VC particles are precipitated and their average size reaches 21 nm, 29 nm and 43 nm for aging at 700 °C, 750 °C and 850 °C, respectively. In these high-temperature aged samples, a number of stacking faults on all four sets of $\{111\}_\gamma$ planes are formed as well.
- The chemical formula of the VC precipitate is determined to be $(V_{0.75}Cr_{0.25})C_{0.70}$ by APT and its lattice parameter is 13.6% larger than that of the γ matrix. The orientation relationship between γ and VC is $[110]_\gamma//[110]_{VC}$ and $(001)_\gamma//(001)_{VC}$, i.e., of cube-cube orientation relationship.
- The as-solution treated sample exhibits relatively low recovery ratios (<50%) for a pre-strain range of 2.3–6.2%. Aging at 650 °C does not improve the shape memory effect. Nevertheless, aging at 700–900 °C significantly improves the shape memory effect, where the recovery ratios are almost twice as high as that of the as-solution treated sample.
- After deformation, the stress-induced martensite plates in the as-solution treated sample are much thicker than those in the high-temperature (700–900 °C) aged samples. In the former, the martensite nucleates from grain boundaries and multiple martensite variants form within each grain. In the latter, only one martensite variant forms within each grain and it nucleates in the following manner: with increasing applied strain more and more stacking faults form on a specific set of $\{111\}_\gamma$ planes and combine with the pre-existing stacking faults on these planes, constructing regularly spaced long stacking faults (2 layers apart), i.e., the ε martensite.
- The VC particles can be cut through by the martensite plates, i.e., the former cannot prevent the propagation of the latter. The orientation relationship between γ and ε is $(\bar{1}11)_\gamma//(0001)_\varepsilon$ and $[110]_\gamma//[2\bar{1}\bar{1}0]_\varepsilon$. Within the martensite plates, a number of stacking faults are present.
- Based on the comparison of the martensite plates between the as-solution treated and the high-temperature aged samples, the formation of the characteristic martensite plates with a single variant and extremely small thickness (<3 nm) in the high-

temperature aged samples is proposed to play the dominant role in improving the shape memory effect.

Appendix A. Supplementary data

Supplementary data related to this article can be found at https://doi.org/10.1016/j.actamat.2018.06.008.

References

[1] K. Otsuka, C.M. Wayman (Eds.), Shape Memory Materials, Cambridge University Press, Cambridge, 1998.
[2] T. Omori, R. Kainuma, Materials science: alloys with long memories, Nature 502 (2013) 42–44.
[3] J. Ma, I. Karaman, R.D. Noebe, High temperature shape memory alloys, Int. Mater. Rev. 55 (2010) 257–315.
[4] J. Perkins, Shape memory behavior and thermoelastic martensitic transformations, Mater. Sci. Eng. 51 (1981) 181–192.
[5] R. Boyer, E.W. Collings, G. Welsch (Eds.), Materials Properties Handbook: Titanium Alloys, 1 ed, ASM International, Materials park, 1994.
[6] K. Otsuka, X. Ren, Physical metallurgy of Ti–Ni-based shape memory alloys, Prog. Mater. Sci. 50 (2005) 511–678.
[7] G.B. Brook, Applications of titanium-nickel shape memory alloys, Mater. Des. 4 (1983) 835–840.
[8] L. Petrini, F. Migliavacca, Biomedical applications of shape memory alloys, J. Metall 2011 (2011).
[9] H. Kahn, M.A. Huff, A.H. Heuer, The TiNi shape-memory alloy and its applications for MEMS, J. Micromech. Microeng. 8 (1998) 213–221.
[10] D. Dye, Shape memory alloys: towards practical actuators, Nat. Mater. 14 (2015) 760–761.
[11] A. Sato, E. Chishima, K. Soma, T. Mori, Shape memory effect in $\gamma \rightleftarrows \varepsilon$ transformation in Fe–30Mn–1Si alloy single crystals, Acta Metall. 30 (1982) 1177–1183.
[12] J.S. Robinson, P.G. McCormick, Factors influencing shape memory behaviour in an Fe–Mn–Si alloy, Scripta Metall. 23 (1989) 1975–1978.
[13] H. Otsuka, H. Yamada, T. Maruyama, H. Tanahashi, S. Matsuda, M. Murakami, Effects of alloying additions on Fe–Mn–Si shape memory alloys, ISIJ Int. 30 (1990) 674–679.
[14] M.M. Reyhani, P.G. McCormick, Mechanical and shape memory behaviour in an Fe–Mn–Si–Cr–Ni alloy, Mater. Sci. Eng., A 160 (1993) 57–61.
[15] M. Murakami, H. Otsuka, S. Matsuda, Improvement in shape memory effect for Fe–Mn–Si alloys, Trans. ISIJ 27 (1987). B89–B89.
[16] Y. Watanabe, Y. Mori, A. Sato, Training effect in Fe–Mn–Si shape-memory alloys, J. Mater. Sci. 28 (1993) 1509–1514.
[17] L.J. Rong, Y.Y. Li, C.X. Shi, Improvement of shape memory effect in an Fe–Mn–Si alloy by prestraining of austenite, Mater. Lett. 21 (1994) 395–397.
[18] D.P. Dunne, H. Li, The mechanism of thermomechanical training of a newly developed Fe–Mn–Si–Cr–Cu shape memory alloy, J. Phys. IV 5 (1995) 415–420.
[19] L.J. Rong, Y.Y. Li, C.X. Shi, Improvement of shape memory effect in an Fe–Mn–Si–Cr–Ni alloy, Scripta Mater. 34 (1996) 993–998.
[20] D. Wang, W. Ji, M. Han, D. Jia, W. Liu, Influence of ausforming on substructures and shape memory behavior in Fe–28Mn–6Si–5Cr alloy, Mater. Sci. Forum 327–328 (2000) 263–266.
[21] S. Kajiwara, D. Liu, T. Kikuchi, N. Shinya, Remarkable improvement of shape memory effect in Fe-Mn-Si based shape memory alloys by producing NbC precipitates, Scripta Mater. 44 (2001) 2809–2814.
[22] S. Kajiwara, D. Liu, Z. T. Kikuchi, N. Shinya, Development of Fe–Mn–Si based shape memory alloys with no necessity of "training, J. Phys. IV France 11 (2001) 199–204.
[23] D. Wang, D. Liu, Z. Dong, W. Liu, J. Chen, Improvement of shape memory effect by ausforming in Fe–28Mn–6Si–5Cr alloy, Mater. Sci. Eng., A 315 (2001) 174–179.
[24] A. Baruj, T. Kikuchi, S. Kajiwara, N. Shinya, Effect of pre-deformation of austenite on shape memory properties in Fe–Mn–Si-based alloys containing Nb and C, Mater. Trans. 43 (2002) 585–588.
[25] A. Baruj, T. Kikuchi, S. Kajiwara, TEM observation of the internal structures in NbC containing Fe–Mn–Si-based shape memory alloys subjected to predeformation above room temperature, Mater. Sci. Eng., A 378 (2004) 337–342.
[26] H. Kubo, K. Nakamura, S. Farjami, T. Maruyama, Characterization of Fe–Mn–Si–Cr shape memory alloys containing VN precipitates, Mater. Sci. Eng., A 378 (2004) 343–348.
[27] F. Susan, H. Kenji, K. Hiroshi, Shape memory effect and crystallographic investigation in VN containing Fe-Mn-Si-Cr alloys, Mater. Trans. 45 (2004) 930–935.
[28] Z.Z. Dong, S. Kajiwara, T. Kikuchi, T. Sawaguchi, Effect of pre-deformation at room temperature on shape memory properties of stainless type Fe–15Mn–5Si–9Cr–5Ni–(0.5–1.5)NbC alloys, Acta Mater. 53 (2005) 4009–4018.
[29] Y.H. Wen, W. Zhang, N. Li, H.B. Peng, L.R. Xiong, Principle and realization of improving shape memory effect in Fe–Mn–Si–Cr–Ni alloy through aligned

precipitations of second-phase particles, Acta Mater. 55 (2007) 6526—6534.

[30] Z. Dong, U.E. Klotz, C. Leinenbach, A. Bergamini, C. Czaderski, M. Motavalli, A novel Fe—Mn—Si shape memory alloy with improved shape recovery properties by VC precipitation, Adv. Eng. Mater. 11 (2009) 40—44.

[31] C. Leinenbach, H. Kramer, C. Bernhard, D. Eifler, Thermo-mechanical properties of an Fe—Mn—Si—Cr—Ni—VC shape memory alloy with low transformation temperature, Adv. Eng. Mater. 14 (2012) 62—67.

[32] Y.H. Wen, H.B. Peng, D. Raabe, I. Gutierrez-Urrutia, J. Chen, Y.Y. Du, Large recovery strain in Fe-Mn-Si-based shape memory steels obtained by engineering annealing twin boundaries, Nat. Commun. 5 (2014) 4964.

[33] S. Kajiwara, Characteristic features of shape memory effect and related transformation behavior in Fe-based alloys, Mater. Sci. Eng., A 273—275 (1999) 67—88.

[34] N. Bergeon, S. Kajiwara, T. Kikuchi, Atomic force microscope study of stress-induced martensite formation and its reverse transformation in a thermomechanically treated Fe—Mn—Si—Cr—Ni alloy, Acta Mater. 48 (2000) 4053—4064.

[35] S. Kajiwara, K. Ogawa, Mechanism of improvement of shape memory effect by training in Fe—Mn—Si-based alloys, Mater. Sci. Forum 327—328 (2000) 211—214.

[36] D.Z. Liu, S. Kajiwara, T. Kikuchi, N. Shinya, Atomic force microscopy study on microstructural changes by 'training' in Fe—Mn—Si-based shape memory alloys, Philos. Mag 83 (2003) 2875—2897.

[37] K. Ogawa, S. Kajiwara, HREM study of stress-induced transformation structures in an Fe—Mn—Si—Cr—Ni shape memory alloy, Mater. Trans., JIM 34 (1993) 1169—1176.

[38] D.Z. Liu, S. Kajiwara, T. Kikuchi, N. Shinya, D.F. Wang, W.X. Liu, Mechanism of the improvement of the shape memory effect by "training" and ausforming in Fe—Mn—Si based shape memory alloys, Mater. Trans., JIM 41 (2000) 593—596.

[39] N. Stanford, D.P. Dunne, Effect of NbC and TiC precipitation on shape memory in an iron-based alloy, J. Mater. Sci. 41 (2006) 4883—4891.

[40] N. Stanford, D.P. Dunne, Effect of second-phase particles on shape memory in Fe—Mn—Si-based alloys, Mater. Sci. Eng., A 454—455 (2007) 407—415.

[41] S. Zaefferer, N.-N. Elhami, Theory and application of electron channelling contrast imaging under controlled diffraction conditions, Acta Mater. 75 (2014) 20—50.

[42] M.J. Lai, C.C. Tasan, D. Raabe, On the mechanism of {332} twinning in metastable β titanium alloys, Acta Mater. 111 (2016) 173—186.

[43] R.K. Ham, The determination of dislocation densities in thin films, Philos. Mag 6 (1961) 1183—1184.

[44] D.B. Williams, C.B. Carter, Transmission Electron Microscopy: a Textbook for Materials Science, second ed., Springer Science+Business Media, 2009.

[45] O.C. Hellman, J.A. Vandenbroucke, J. Rüsing, D. Isheim, D.N. Seidman, Analysis of three-dimensional atom-probe data by the proximity histogram, Microsc. Microanal. 6 (2000) 437—444.

[46] L. Jian, C.M. Wayman, On the mechanism of the shape memory effect associated with γ(fcc) to ε(hcp) martensitic transformations in Fe—Mn—Si based alloys, Scripta Metall. Mater. 27 (1992) 279—284.

[47] J.R. Patel, K.A. Jackson, H. Reiss, Oxygen precipitation and stacking-fault formation in dislocation-free silicon, J. Appl. Phys. 48 (1977) 5279—5288.

[48] J.S.T. Van Aswegen, R.W.K. Honeycombe, Segregation and precipitation in stacking faults, Acta Metall. 10 (1962) 262—264.

[49] J.M. Silcock, W.J. Tunstall, Partial dislocations associated with NbC precipitation in austenitic stainless steels, Philos. Mag 10 (1964) 361—389.

[50] J.S.T. Van Aswegen, R.W.K. Honeycombe, D.H. Warrington, Precipitation on

[51] J.J. Irani, R.T. Weiner, Precipitation of vanadium carbide on stacking faults, Nature 205 (1965), 795—795.

[52] F.H. Froes, B.W.K. Honeycombe, D.H. Warrington, Conditions controlling matrix and stacking fault precipitation, Acta Metall. 15 (1967) 157—159.

[53] K. Kamei, Y. Maehara, Y. Ohmori, Effect of stacking fault precipitation on hot deformation of austenitic stainless steel, Trans. ISIJ 26 (1986) 159—166.

[54] S. Farjami, H. Kubo, Elastic energy analysis of carbide and nitride-type precipitates in an Fe—Mn—Si—Cr shape memory alloy, Mater. Trans. 47 (2006) 564—570.

[55] M. Kuzmina, M. Herbig, D. Ponge, S. Sandlöbes, D. Raabe, Linear complexions: confined chemical and structural states at dislocations, Science 349 (2015) 1080—1083.

[56] T. Hickel, S. Sandlöbes, R.K.W. Marceau, A. Dick, I. Bleskov, J. Neugebauer, D. Raabe, Impact of nanodiffusion on the stacking fault energy in high-strength steels, Acta Mater. 75 (2014) 147—155.

[57] H. Suzuki, Segregation of solute atoms to stacking faults, J. Phys. Soc. Jpn. 17 (1962) 322—325.

[58] S.K. Dhua, D. Mukerjee, D.S. Sarma, Effect of cooling rate on the as-quenched microstructure and mechanical properties of HSLA-100 steel plates, Metall. Mater. Trans. A 34 (2003) 2493—2504.

[59] E.K. Storms, C.P. Kempter, Thermal expansion of some vanadium carbides, J. Chem. Phys. 42 (1965) 2043—2045.

[60] C. Czaderski, M. Shahverdi, R. Brönnimann, C. Leinenbach, M. Motavalli, Feasibility of iron-based shape memory alloy strips for prestressed strengthening of concrete structures, Construct. Build. Mater. 56 (2014) 94—105.

[61] N. Bergeon, G. Guenin, C. Esnouf, Microstructural analysis of the stress-induced ε martensite in a Fe—Mn—Si—Cr—Ni shape memory alloy: Part I—calculated description of the microstructure, Mater. Sci. Eng., A 242 (1998) 77—86.

[62] N. Bergeon, G. Guenin, C. Esnouf, Microstructural analysis of the stress-induced ε martensite in a Fe—Mn—Si—Cr—Ni shape memory alloy: Part II: transformation reversibility, Mater. Sci. Eng., A 242 (1998) 87—95.

[63] B.C. Maji, M. Krishnan, A. Verma, R. Basu, I. Samajdar, R.K. Ray, Effect of pre-straining on the shape recovery of Fe-Mn-Si-Cr-Ni shape memory alloys, Metall. Mater. Trans. A 46 (2015) 639—655.

[64] Q. Qin, S. Yin, G. Cheng, X. Li, T.-H. Chang, G. Richter, Y. Zhu, H. Gao, Recoverable plasticity in penta-twinned metallic nanowires governed by dislocation nucleation and retraction, Nat. Commun. 6 (2015) 5983.

[65] S.L. Wong, M. Madivala, U. Prahl, F. Roters, D. Raabe, A crystal plasticity model for twinning- and transformation-induced plasticity, Acta Mater. 118 (2016) 140—151.

[66] J. Wang, N. Li, O. Anderoglu, X. Zhang, A. Misra, J.Y. Huang, J.P. Hirth, Detwinning mechanisms for growth twins in face-centered cubic metals, Acta Mater. 58 (2010) 2262—2270.

[67] T. Kikuchi, S. Kajiwara, Y. Tomota, Microscopic studies on stress-induced martensite-transformation and its reversion in an Fe—Mn—Si—Cr—Ni shape-memory alloy, Mater. Trans., JIM 36 (1995) 719—728.

[68] C. Leinenbach, A. Arabi-Hashemi, W.J. Lee, A. Lis, M. Sadegh-Ahmadi, S. Van Petegem, T. Panzner, H. Van Swygenhoven, Characterization of the deformation and phase transformation behavior of VC-free and VC-containing FeMnSi-based shape memory alloys by in situ neutron diffraction, Mater. Sci. Eng., A 703 (2017) 314—323.